Zhang et al. *NPG Asia Materials* (2023) 15:58
https://doi.org/10.1038/s41427-023-00505-9

NPG Asia Materials

ARTICLE Open Access

Visualizing the spatial distribution of inflammation in the depressed brain with a targeted MRI nanoprobe in vivo

Peisen Zhang[1,2], Jiaoqiong Guan[1,3,4], Ni Zhang[5], Lichong Zhu[2], Yu Wang[2], Wenyue Li[2], Zhe Shi[6], Xueyuan Liu[3], Xue Li[1,3], Meng Qin[2,5], Yi Hou[2] and Yue Lan[1,7]

Abstract

Depression is a prevalent mental illness that imposes a substantial public health burden. However, the diverse clinical phenotypes observed in patients make it difficult to realize precise diagnosis. Recently, accumulating preclinical and clinical evidence has suggested that inflammation is involved in the pathophysiology of depression. Herein, a molecular imaging–based strategy was proposed as a means to diagnose depression precisely by specifically visualizing the inflammation status associated with depression. Inflammation-targeting MRI nanoprobes were constructed by attaching an intercellular cell adhesion molecule-1 (ICAM-1)-targeting peptide to biocompatible Fe_3O_4 nanoparticles. Systematic studies demonstrated that the nanoprobes could specifically target inflamed vascular endothelial cells and visualize the spatial distribution of inflammation in the depressed brain in vivo through susceptibility-weighted imaging (SWI), which was further confirmed by histological analysis. Additionally, these inflammatory brain regions identified by nanoprobe-based imaging are consistent with the focal regions closely associated with the symptoms of depression as reported in previous behavioral studies. Overall, this is the first study to directly visualize the distribution of inflammation in the depressed brain in vivo through a molecular imaging strategy, which may not only facilitate insight into the biological mechanism underlying depression but also provide a potential target within the depressed brain for the further development of anti-inflammatory therapies.

Introduction

Depression, afflicting ~5–9% of the population at any time, is one of the most common mental illnesses and has a high lifetime prevalence that imposes a substantial public health burden[1,2]. People with depression usually exhibit typical depressive symptoms and negative cognitive functioning, such as mood disturbance and anhedonia, cognitive distortions, negative attributions, hopelessness, low self-esteem, and even psychotic features or suicidal ideation[3].

Although most types of depression can be effectively controlled by early clinical intervention, the effective management of depression still faces many challenges. On the one hand, the delayed diagnosis of depression may lead to delayed treatment, thus prolonging the suffering of patients and increasing the risk of hazardous events[4]. On the other hand, improper treatment due to misdiagnosis of depression may produce unsatisfactory clinical outcomes, resulting in aggravation of the condition[5]. In this context, a timely and accurate diagnosis of depression is of great significance in depression management, which is a crucial prerequisite for effective treatment.

In the clinic, the diagnosis of depression mainly depends on anxiety symptoms, medical history, and contextual

Correspondence: Yue Lan (bluemooning@163.com)
[1]Department of Rehabilitation Medicine, Guangzhou First People's Hospital, School of Medicine, South China University of Technology, 510180 Guangzhou, Guangdong, China
[2]College of Life Science and Technology, Beijing University of Chemical Technology, 100029 Beijing, China
Full list of author information is available at the end of the article
These authors contributed equally: Peisen Zhang, Jiaoqiong Guan

factors[6]. Relative scales, such as the Patient Health Questionnaire-9 (PHQ-9)[7], Hopkins Symptom Checklist Depression Scale (HSCL-D)[8], and Hospital Anxiety and Depression Scale (HADS)[9], have been developed for screening patients with anxiety and depression from normal individuals. Through these evaluation scales, some types of depression can be diagnosed and preliminarily categorized by the different score ranges. However, depression usually presents a large clinical phenotype that varies from person to person and is difficult to assess through simply using cutoff scores on rating scales[10]. In addition, patients with depressive diseases usually present in the depressive phase, especially the elderly population, who are easily affected by uncertain emotions to provide inaccurate feedback[11]. Under this circumstance, the diagnostic reliability of the simple scale evaluation may be unsatisfactory, since various heterogeneous populations may be included in the same category. To overcome these limitations, new approaches that take an objective biological measurement, especially at the molecular or cellular level, may be useful to detect a more homogeneous subpopulation of patients with depression.

Molecular imaging techniques offer possibilities to visualize the targets of diseases through molecular recognition of the imaging nanoprobe, which has been demonstrated to be effective for diagnosing malignant tumors[12,13], atherosclerotic plaques and thrombosis[14,15], and cerebral ischemic stroke[16–18], but rarely for evaluating depression. In comparison with the clinical scales that depend on the recognition of a constellation of signs and symptoms derived from the ambiguous and subjective description of patients, molecular imaging is able to provide objective and direct evidence for diseases at the molecular level. On this basis, it is necessary to develop an advanced molecular imaging approach to improve the detection of depression, which is expected to specifically image the depressive status of the brain by specifically targeting the relevant pathological molecules. This approach may ultimately allow clinicians to provide molecular mechanism-based treatment interventions for patients with depression.

Although the mechanism of depression is not fully understood, accumulating preclinical and clinical evidence has suggested in recent years that inflammation is involved in the pathophysiology of depression[19,20]. Specifically, it has been demonstrated that the expression levels of proinflammatory cytokines and their receptors are upregulated in the peripheral blood and cerebrospinal fluid of patients with depressive disorder. In addition, a variety of innate immune molecules, including interleukin (IL)-6, tumor necrosis factor (TNF)-α, Toll-like receptor (TLR) 3 and TLR4, and intercellular cell adhesion molecule-1 (ICAM-1), have been found to be upregulated in postmortem brain samples from depression patients[21–23]. Very recently, fMRI has revealed that inflammatory stimuli can vary the molecular metabolic pathways, thus influencing the neurotransmitter system and ultimately affecting the neural circuits and networks that regulate motivation reduction, avoidance, and alarm[24,25]. The above-sophisticated correlation between depression and inflammation suggests that inflammatory markers might be used as appropriate molecular targets for depression, regardless of diagnosis or treatment. Nevertheless, the direct visualization of inflammation status associated with a depressed brain in vivo, which is very challenging but of great significance, has rarely been reported.

In the current work, a molecular imaging strategy was proposed for precisely visualizing the inflammation status associated with the depressed brain. In our recent study, we found that Fe_3O_4 nanoparticle-based susceptibility-weighted imaging (SWI) can be employed to detect acute ischemic stroke with outstanding imaging resolution and sensitivity, especially mapping the abnormal enlargement, anastomosis, and leakage of brain vessels[16,17]. Nevertheless, it is challenging to accurately diagnose depression through anatomical structural imaging, as most depressed brains do not exhibit obvious organic brain disorders. In this context, the molecular imaging strategy proposed herein shifts the focus of imaging from nonspecific anatomical structures to specific pathological molecules of the depressed brain, thereby achieving a precise diagnosis of depression. In detail, an inflammation nanoprobe was designed by coating the ICAM-1 targeting peptide on biocompatible Fe_3O_4 nanoparticles. The working mechanism of the nanoprobes is shown in Scheme 1. cLABL, a cyclic decapeptide derived from the I-domain of the a-subunit of lymphocyte function-associated antigen-1 (LFA-1) that has been demonstrated to be the specific ligand of the ICAM-1 receptor (Fig. S1), was chosen as the targeting molecule for cerebral inflammation[26,27]. Owing to the targeting ability of the cLABL peptide, the probes can specifically bind with the upregulated ICAM-1 receptors on the surface of inflamed vascular endothelial cells. With such a design, the nanoprobes are expected to continuously accumulate in the inflammatory region of the depressed brain, resisting rapid elimination from the bloodstream. Through this molecular imaging strategy, the spatial distribution of inflammation in the depressed brain is expected to be visualized at the molecular level. In the experiments reported below, in vitro and in vivo studies will be carried out to validate the specific diagnostic ability of the nanoprobe for depression. This will be the first study to directly delineate the inflammatory region of the depressed brain in vivo through a molecular imaging strategy.

Results

Construction and characterization of an inflammation-targeting nanoprobe

The depression-associated inflammation nanoprobe shown in Fig. 1a was established by modifying the cyclic peptide cLABL on the surface of Fe_3O_4 nanoparticles

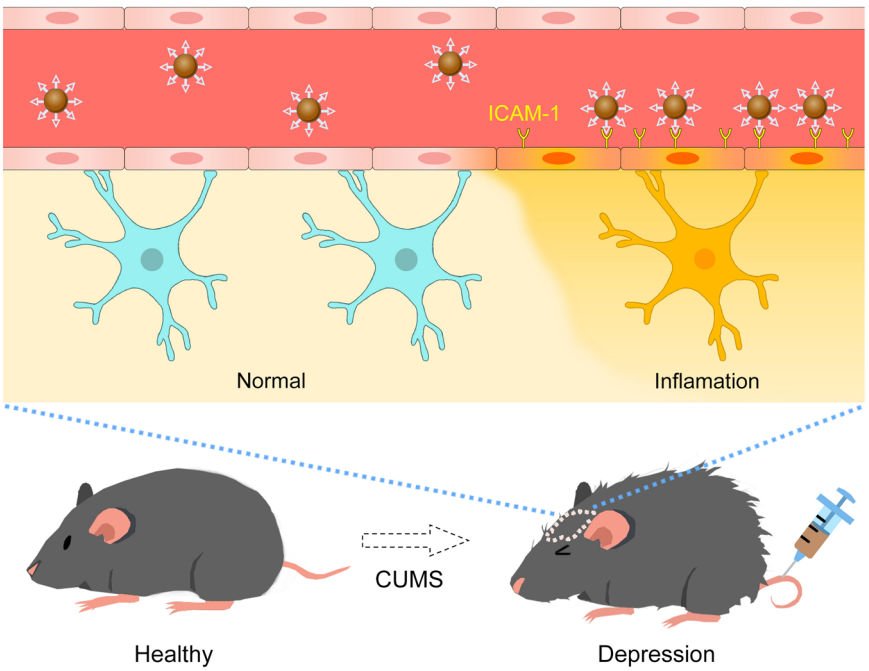

Scheme 1 Schematic illustration to demonstrate the visualization of the special distribution of inflammatory status in the depressed brain by ICAM-1-targeting MRI nanoprobes.

(NPs). Specifically, oleate-capped Fe_3O_4 NPs (Fig. S2) were synthesized using a previously reported thermal decomposition route[17,28]. By exchanging the oleate ligand with an asymmetric polyethylene glycol (PEG) ligand containing a diphosphonate and a maleimide group on the two terminals (known as dP–PEG–Mal), biocompatible PEGylated Fe_3O_4 NPs were obtained (Fig. 1b). Thereafter, to attach the cLABL peptides to the surface of biocompatible Fe_3O_4 NPs, Traut's reagent was employed to react with the primary amine of the peptide in a ring-opening reaction to regenerate a free sulfhydryl group available for further coupling. Subsequently, the sulfhydrylated cLABL peptide molecules were reacted with the maleimide residues on the terminus of surface PEG ligands through click reactions, thereby forming a stable linkage and acquiring the desired depression inflammation nanoprobes (Fig. 1c).

The size distributions of oleate-capped Fe_3O_4 NPs, PEGylated Fe_3O_4 NPs and inflammation nanoprobes were analyzed by counting the sizes of the individual particles within the transmission electron microscope (TEM) images. The results are displayed in Figs. S3–S5 in the Supplementary Information (SI). According to the histograms, the average core diameters of these three particles were 15.5 ± 1.8, 15.4 ± 1.8, and 15.6 ± 1.9 nm, respectively, indicating that the average core sizes of Fe_3O_4 nanoparticles remained unchanged after the ligand exchange and peptide modification procedures.

To further investigate the influence of the surface modification procedure on the properties of biocompatible PEGylated Fe_3O_4 NPs, the surface charges of nanoparticles were measured before and after peptide conjugation. As shown in Fig. 1d, the zeta potential of the PEGylated Fe_3O_4 NPs decreased from 12.4 to −0.2 mV after the conjugation of peptide molecules. The zeta potential decrease can be attributed to the multiple free negatively charged carboxylic groups of the cLABL peptide molecule. This charge variation strongly confirmed that the cLABL peptide molecules were successfully attached to the surface of biocompatible Fe_3O_4 NPs and the desired inflammation-targeted nanoprobes were successfully obtained.

The water solubility of nanoprobes is crucial for their potential biomedical applications. To assess the monodispersity of nanoprobes in aqueous solution, dynamic light scattering (DLS) was conducted. As shown in Fig. 1e, the size of the NPs in the water solution, as indicated by the number-weighted hydrodynamic diameter (D_h), increased from 21.7 to 24.4 nm after peptide modification. In comparison with the average size measured in TEM images, this larger D_h of NPs in water is consistent with the reported length of the PEG-peptide conjugate ligands[29]. Importantly, the shape of the distribution curve of nanoprobes was symmetrical without trailing, implying that peptide conjugation occurred in a controllable manner, resulting in the high water monodispersity of nanoprobes. In addition to the D_h measurement, the

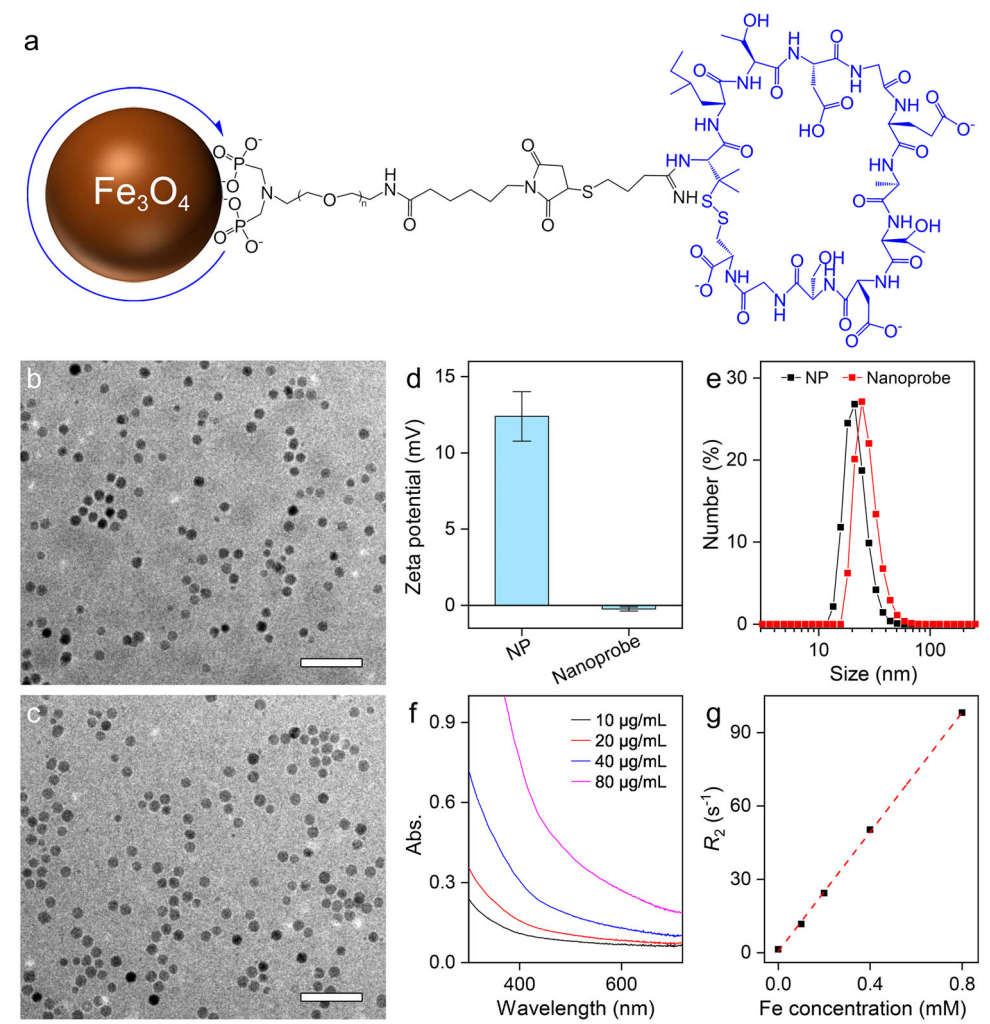

Fig. 1 Construction and characterization of the inflammation-targeting nanoprobe. a Schematic illustration showing the molecular structure of the nanoprobe. TEM images of **b** PEGylated Fe_3O_4 NPs and **c** nanoprobes (the embedded scale bar corresponds to 100 nm). **d** Zeta potentials of NPs and nanoprobes. **e** Hydrodynamic size distribution profiles of NPs and nanoprobes. **f** UV–Vis absorption spectrum of an aqueous solution of nanoprobes. **g** R_2 values of aqueous solutions of nanoprobes with different Fe concentrations, together with the corresponding linear fittings for extracting the r_2 of nanoprobes.

water solubility of the nanoprobes was also assessed based on their absorbance properties. As illustrated in Fig. 1f, the aqueous solution of nanoprobes with different concentrations showed a broad absorption spectrum without obvious distinct features, covering almost the entire visible region. Even so, it is worth noting that the UV–Vis absorbance spectra of the nanoprobes exhibited a strongly concentration-dependent feature in accordance with the Lambert–Beer law, as evidenced by the high correlation coefficient of 0.98 (Fig. S6). This result indicates that the nanoprobes did not precipitate even at high concentrations, confirming the good water solubility of the nanoprobes.

In addition to the structural characterization, the in vitro MRI performance of the nanoprobes was further assessed. Due to the superparamagnetism property of core Fe_3O_4 NPs, it was expected that the nanoprobes would exhibit a strong T_2 contrast enhancement effect. As displayed in Fig. 1g, the transverse relaxivity R_2 values of aqueous solutions of nanoprobes at different concentrations (with respect to Fe) were measured. By performing linear regression analysis of these R_2 values, the transverse molar relaxivity r_2 of the nanoprobe was determined to be 122.1 $mM^{-1}\,s^{-1}$. Using a similar approach, the longitudinal molar relaxivity r_1 of the nanoprobe was extracted as 0.73 $mM^{-1}\,s^{-1}$ based on the slope of the regression curve (Fig. S7). Therefore, the r_2/r_1 ratio of the nanoprobes reached 167. Consequently, the high r_2 values, as well as the high r_2/r_1 ratio, render the current nanoprobes excellent candidates for T_2 contrast agents. Additionally,

to display the SWI performance of the nanoprobes, T_2*-weighted imaging (T_2*WI) and SWI of a series of aqueous solutions of nanoprobes were carried out. As shown in Fig. S8, the nanoprobes exhibited significant Fe concentration-dependent T_2* and SWI contrast enhancement effects, significantly darkening their aqueous solutions in T_2*WI and SWI. These results indicated that the current nanoprobe can serve as not only a T_2 contrast agent but also a satisfactory T_2* and SWI contrast agent.

Binding affinity and cytotoxicity of nanoprobes in vitro

Maintaining the targeting ability of the cLABL peptide is of utmost importance for the subsequent biomedical application of the resulting nanoprobes. Therefore, the inflammation-targeting ability of nanoprobes was quantitatively assessed through Perl's staining cell binding assays (Fig. 2a). Lipopolysaccharide (LPS)-activated human umbilical vein endothelial cells (HUVECs) were used as positive cell models to simulate inflamed vascular endothelial cells in the depressed brain, while non-activated HUVECs were used as negative cell models to simulate normal endothelial cells in the healthy brain. The binding behaviors of the nanoprobes and Fe_3O_4 NPs to HUVECs with different activation statuses were qualitatively detected by Perl's staining, as shown in Fig. 2b. The staining results clearly demonstrated that the nanoprobes actively targeted LPS-activated HUVECs, while the nanoprobes did not show specific binding affinity to nonactivated HUVECs. Additionally, the targeting ability of Fe_3O_4 NPs to either LPS-activated or nonactivated HUVECs was not evident, indicating that the nonspecific uptake of the Fe_3O_4 NPs without targeting abilities is rather weak. To further quantify the results, the integral of blue signals in three different fields of view of optical microscope images with similar cell densities were averaged. The analysis revealed that the amount of nanoprobe bound to LPS-activated HUVECs was over 60 times higher than that of nonactivated HUVECs after incubation ($p < 0.001$), as shown in Fig. 2c. This quantitative statistic confirmed that the nanoprobes have satisfactory binding specificity to inflamed vascular endothelial cells that overexpress ICAM-1 receptors on the membranes. Additionally, the weak binding affinity of the PEGylated NPs provides strong evidence that the binding specificity of the nanoprobes is mainly due to the specific interaction between the cLABL peptide and the ICAM-1 receptor.

It is widely accepted that an ideal contrast agent should be nontoxic or have low toxicity to normal cells to avoid adverse side effects. To confirm the biosafety of the nanoprobes at the cellular level, the cytotoxicity of the nanoprobes was assessed in HUVECs by Cell Counting Kit-8 (CCK-8) assays. As shown in Fig. 2d, the CCK-8 results indicated that the current nanoprobes exhibited minimal cytotoxicity when the Fe concentration was below 2.5 mM. This probe concentration is comparable to the maximal blood concentration in the subsequent in vivo imaging studies. In addition to assessing cytotoxicity, the hemocompatibility of the nanoprobes was also considered. Specifically, the hemolysis rates (HRs) of nanoprobes in normal saline (NS) solution with different Fe concentrations ranging from 0.01 to 5 mM were calculated, with RBCs in pure water and NS serving as the positive control (100% HR) and negative control (0% HR), respectively. As indicated in Fig. 2e, the HR of the nanoprobe solutions, as calculated using the formula in the experimental section, was found to be lower than 5%, which is the upper limit specified by the American Society for Testing and Materials (ASTM). Considering the results of the cytotoxicity assays and hemolysis rate together, it can be reasonably concluded that the nanoprobe satisfies the biosafety prerequisite for an intravenously injected agent.

Establishment of a chronic unpredictable mild stress mouse model of depression

To validate the potential of the current nanoprobe in targeting the inflammatory region of the depressed brain by interacting with ICAM-1, a mouse model of depression was established using chronic unpredictable mild stress (CUMS) induction, which is often utilized in laboratory animals to mimic the unpredictable life stressors and life adversity that may contribute to the development of major depressive disorder in humans[30]. In detail, 10 healthy C57BL/6J mice were randomly divided into two groups ($n = 5$). One group of mice was exposed to a variety of mild stressors, including food deprivation, forced swimming, water deprivation, chronic restraint stress, 45° cage tilt, clipping the tail, a damp cage, foot shock, and overnight illumination, for a period of 7 weeks to establish the CUMS-induced depression mice models (Fig. 3a). The other group of mice was set as the controls without CUMS exposure and were only handled 5 minutes per day.

To evaluate the degree of depression among the mice, several behavioral tests were carried out, including the sucrose preference test (SPT), open field test (OFT), and tail suspension test (TST). These tests were performed on every mouse one day after the CUMS procedure (Fig. 3b–d), aiming to measure the behavioral endpoints in model animals. In comparison with the control mice, the mice in the CUMS group exhibited increased depression-like symptoms, such as anhedonia, despair, and anxiety-like behaviors. As indicated in Fig. 3e–g, the mice in the CUMS group exhibited a marked reduction in sucrose preference compared to the control mice in the SPT ($p < 0.01$). Apart from sucrose preference, no significant difference was observed in the ratio of time spent

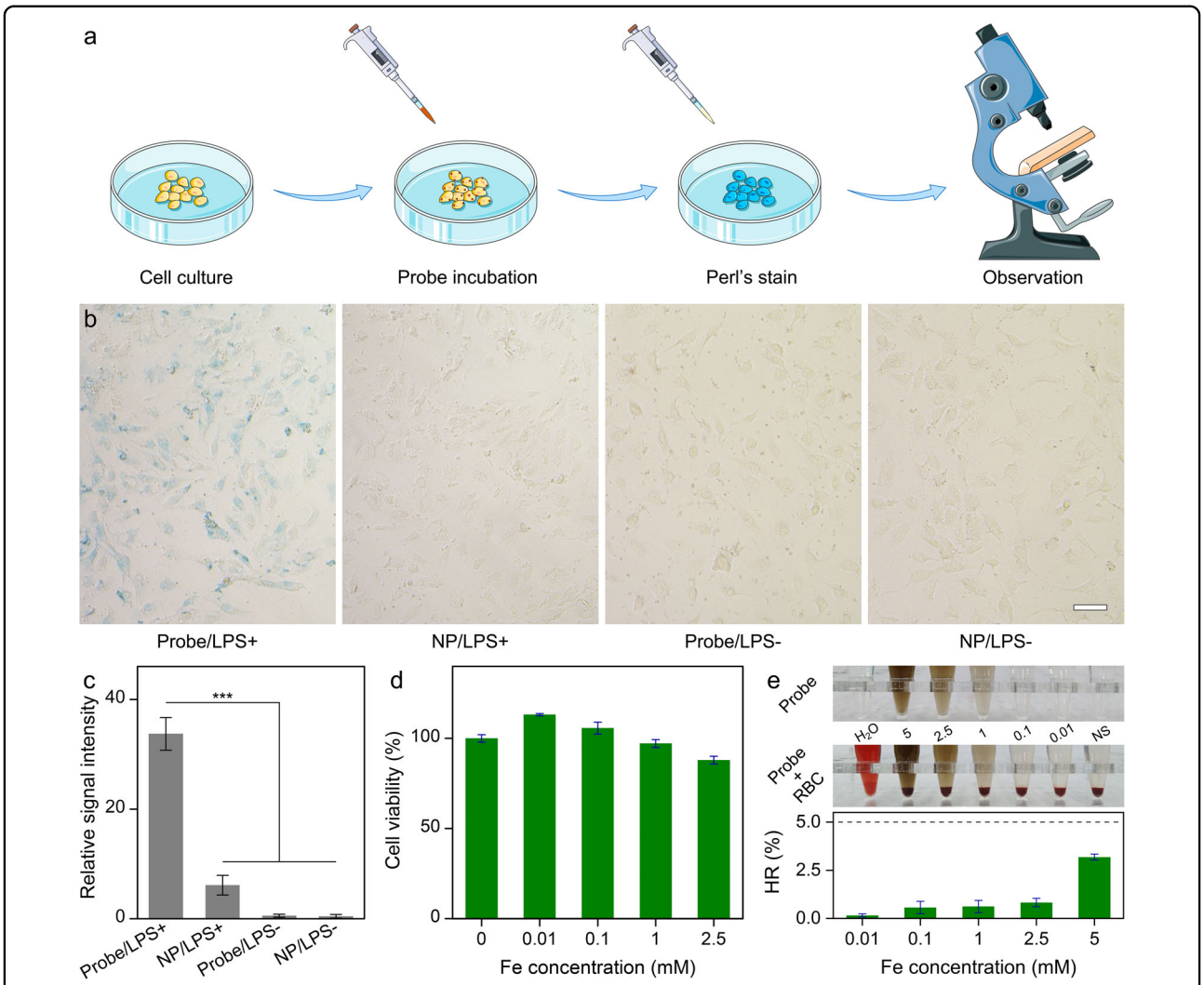

Fig. 2 Binding affinity and cytotoxicity of nanoprobes in vitro. a Schematic illustration showing the cell binding affinity assays. **b** Microscopy image of HUVECs obtained after Perl's Prussian blue staining for showing the Fe contents (the embedded scale bar corresponds to 100 μm), and **c** integrated blue signals for quantitatively showing the binding affinity of probes and NPs to HUVECs in the presence or absence of LPS. Data are shown as the mean ± SD. Statistical significance was determined by one-way ANOVA with Tukey's post hoc test (***$p < 0.001$). **d** Viabilities of HUVECs treated with nanoprobes or control NPs with different Fe concentrations. **e** Upper: photographs of nanoprobe solutions with different Fe concentrations with or without red blood cells (RBCs) after centrifugation. Lower: hemolysis rate (HR) of nanoprobes with different Fe concentrations.

in the center zone to the periphery in the OFT, suggesting that the CUMS procedure did not affect the locomotor activity of mice. Moreover, the average immobility time of the mice in the TST was significantly reduced after CUMS exposure ($p < 0.01$).

To further analyze the interrelationships among these ethological indices, linear correlations analyses were used to evaluate the correlations between each pair of tests. As shown in Fig. 3h–j, there was a slight negative correlation between the sucrose preference in the SPT and immobile time in the TST, but no obvious correlation existed between the SPT and OFT or TST and OFT. Notably, through cluster analysis, the data points derived from depression mice and control mice can be well clustered into two different groups under all three coordinate systems, suggesting that there are significant and distinguishable behavioral differences between the depressed mice and the normal mice.

Hence, these results provide strong evidence that the CUMS-induced depressed mouse models were successfully established.

In vivo visualization of inflammation in the depressed brain through MRI

On the basis of the successful establishment of the CUMS-induced depressed mouse model, the potential of the nanoprobe in visualizing inflammation in the depressed brain was validated in vivo (Fig. 4a).

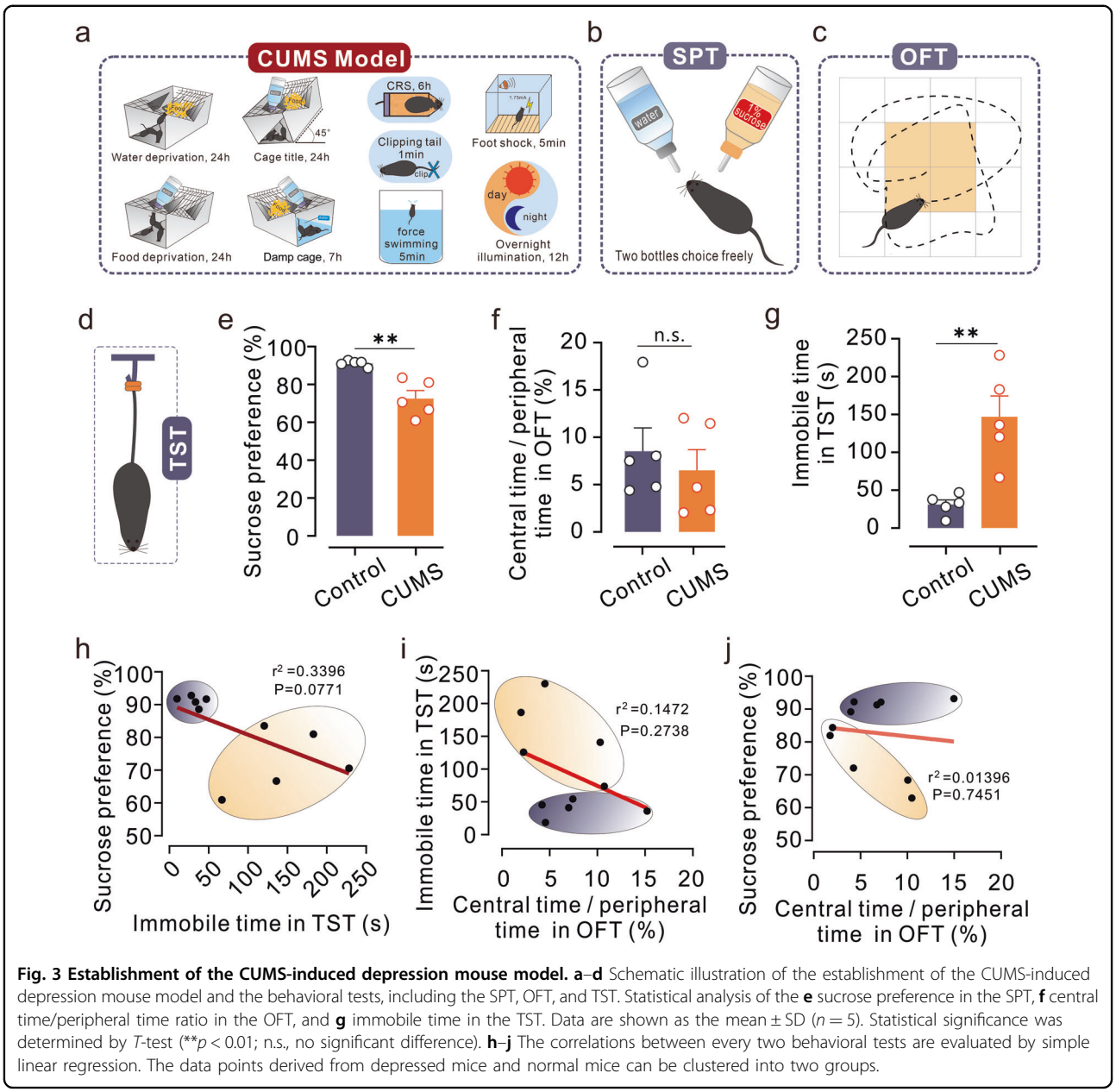

Fig. 3 Establishment of the CUMS-induced depression mouse model. a–d Schematic illustration of the establishment of the CUMS-induced depression mouse model and the behavioral tests, including the SPT, OFT, and TST. Statistical analysis of the **e** sucrose preference in the SPT, **f** central time/peripheral time ratio in the OFT, and **g** immobile time in the TST. Data are shown as the mean ± SD ($n = 5$). Statistical significance was determined by *T*-test (**$p < 0.01$; n.s., no significant difference). **h–j** The correlations between every two behavioral tests are evaluated by simple linear regression. The data points derived from depressed mice and normal mice can be clustered into two groups.

Before the injection of the current targeting nanoprobes, the brains of mice with depression were initially imaged through clinically used MRI sequences. T_1-weighted imaging (T_1WI) has been widely adopted as the basic imaging sequence for revealing cerebral anatomy. As shown in Fig. S9, no obvious anatomical abnormality was observed in the depressed brain, suggesting that depression is inconspicuous in T_1WI. Apart from T_1WI, T_2-weighted imaging (T_2WI) has also been demonstrated to be able to visualize the edema region due to longer T_2 relaxation times of the free water molecules in edema. Fig. S10 shows that no abnormal hyperintense regions were found in the depressed brain, indicating the absence of edema. Apart from T_1WI and T_2WI, T_2*-weighted imaging (T_2*WI), which is a type of gradient-echo (GRE) sequence of MRI that has been used to detect brain microbleeds in clinical settings, was utilized for brain imaging in depressed mice. As shown in Fig. S11, no bleeding points were observed in any region of the depressed brain. The findings indicate that it is difficult to accurately diagnose depression solely based on these commonly used clinical MRI sequences because the depressed brain does not exhibit obvious organic brain disorders.

Susceptibility-weighted imaging (SWI) sequence is a special type of T_2*WI sequence that maximizes the

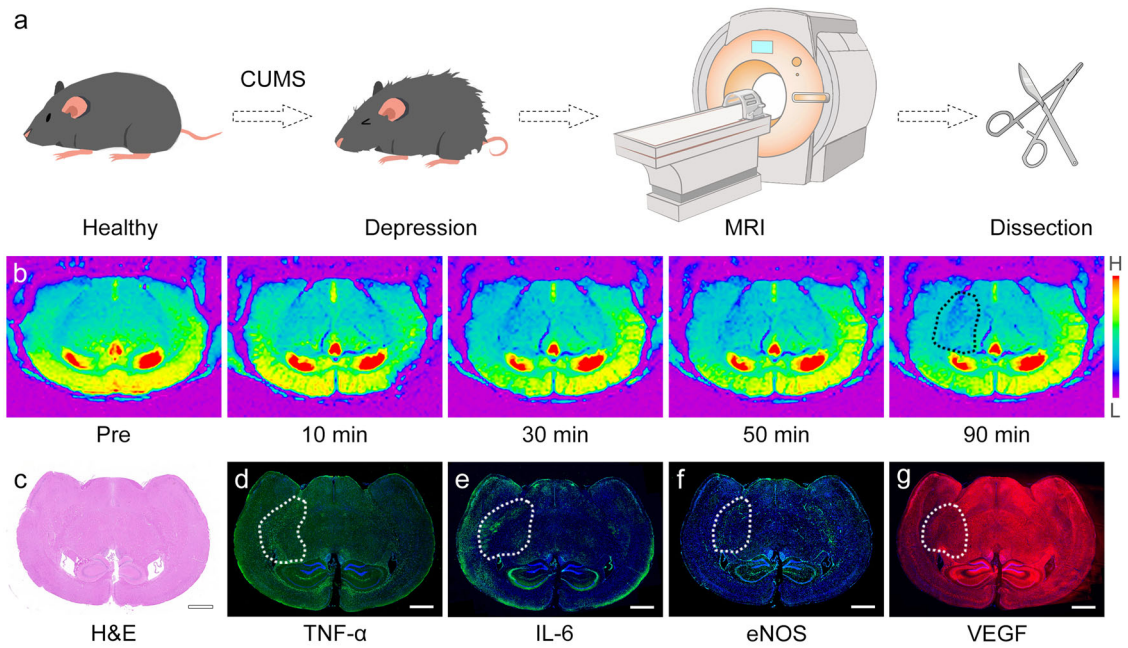

Fig. 4 In vivo inflammation mapping of the depressed brain with MRI. a Schematic illustration of the MRI study procedures of depressed mice. **b** Cerebral SWI of depressed mice recorded before and at different time points after intravenous injection of the nanoprobes (10 mg Fe per kg body weight). **c**–**g** Histopathological analysis of the slices of excised brain tissues through H&E, TNF-α, IL-6, eNOS, and VEGF staining to show the cell morphology and inflammatory status. The embedded scale bars in c-g correspond to 1 mm.

sensitivity to susceptibility effects by combining a long-echo time (TE), fully flow-compensated, GRE sequence with filtered phase information in each voxel to display the differences in susceptibility between different tissues. Fe_3O_4 nanoparticle-based nanoprobes, due to their unique superparamagnetism, can significantly reduce the T_2* relaxation time of water protons and thus can be used as excellent contrast agents for SWI. In this context, with the inflammation-targeting capability of nanoprobes, nanoprobe-enhanced SWI is expected to enable the specific visualization of potential inflammatory regions in the depressed brain with high spatial resolution. SWI images were acquired before and at different time points after intravenous injection of the nanoprobes. Representative images recorded at 10, 30, 50, and 90 min postinjection were selected to demonstrate the temporal evolution of the SWI signals enhanced by the nanoprobes. As shown in Fig. 4b, the intravenous injection of nanoprobes resulted in a strong enhancement of vascular contrast in the cerebral cortex and thalamus at 10 min postinjection, which continued to increase over time until 30 min postinjection. These vascular signals were sustained for at least 90 min. In addition to these nonspecifically anatomical vascular signals, interestingly, an enhanced SWI signal gradually appeared asymmetrically in the right hemisphere after administration of nanoprobes, as indicated by the black dashed circle. This enhancement could be observed from 30 min postinjection and continued to become stronger over time, reaching its peak at 90 min postinjection. According to the atlas of the coronal plane of the mouse brain regions shown in Fig. S12, this enhanced SWI signal was primarily located between the cortex (CTX) and thalamus (TH), covering the lateral hypothalamus (HY), thalamic reticular nucleus (TRN), and lateral globus pallidus regions (LGP). Comparing the same brain region on the contralateral side, the asymmetric signals exhibited a typical dotted distribution around the blood vessels, suggesting their association with inflamed vasculatures. Importantly, the gradual cumulative enhancement of the SWI signals indicated that the nanoprobes accumulated in the corresponding area through inflammation targeting despite blood clearance. In addition, it has been reported that the lateral HY, TRN, and LGP regions highlighted by nanoprobes in SWI are closely associated with depression-like symptoms such as anhedonia, immobility, or mood disorders[31,32]. In particular, lateral HY and TRN have been suggested as potential target regions for the treatment of depression[33,34]. Considering these findings, it is reasonable to believe that the interaction between the surface cLABL peptide on the nanoprobes and ICAM-1 receptors on activated vascular endothelial cells allows the nanoprobes to specifically visualize the inflamed regions of the depressed brain. These regions are crucial in

understanding depression and should be the focus of further research and treatment strategies. Therefore, the current targeting nanoprobe-based molecular MRI strategy allows for the observation of not only the nonspecific anatomical structures of the brain vessels but also the specific pathological inflammation-related molecular information of the depressed brain. This novel strategy emphasizes the shift in imaging focus from nonspecific anatomical properties to the specific pathological molecular sources in the brain, thus enabling the accurate diagnosis of depression.

To further validate the correlation between the SWI signal and inflammation status in the depressed brain, histological studies were conducted on mouse brain slices after MRI. Fig. 4c–g shows that there were no observable morphological structural changes in the brain slices when stained with H&E. However, the expression of TNF-α and IL-6 was specifically upregulated in the lateral HY, TRN, and LGP regions. Conversely, the activity of eNOS and VEGF expression in these brain regions was correspondingly reduced (as identified by the white dashed circles). These abnormal regulations of inflammation- and vascular-related biomarkers observed in the histological analysis are consistent with the reported pathophysiological characteristics of depression[24,35,36], suggesting that depression may lead to a proinflammatory response in the brain, which, in turn, initiates ischemic events[37]. Therefore, the abnormal region indicated by histological studies is consistent with the signal-enhanced region in SWI, strongly confirming that the nanoprobes can precisely reflect the focal inflammation region of the depressed brain. Importantly, the histological analysis further highlighted the major challenges and difficulties in accurately detecting depression solely based on morphological structure. It is evident that even when the morphology remains unchanged, there are significant alterations in molecular expression patterns in the depressed brain. These changes in molecular expression can be utilized as specific markers for the detection of depression through molecular imaging and histological studies.

Biosafety assessment of the nanoprobe

The biosafety of contrast agents is very important, especially for nanosized agents. In clinical practice, several types of iron oxide nanoparticles have been approved by the US Food and Drug Administration (FDA) after careful analysis of their biosafety features by different researchers and clinicians[38,39]. Additionally, we have previously demonstrated the biosafety of various Fe_3O_4 nanoparticle-based nanoprobes[16,28].

The in vitro cellular biosafety of the nanoprobes used in this study was evaluated in the previous section. To further verify the in vivo biosafety of the nanoprobes, depressed mice were sacrificed after MRI experiments. The major organs of the mice were obtained, sliced, embedded in paraffin, and stained with H&E. As controls, H&E staining was also performed on slices from the major organs of a healthy mouse. As shown in Fig. S13, no apparent injury or abnormal morphological changes were observed in any major organs. This histological analysis result suggests that the nanoprobe does not cause undesired pathological changes to the major organs at this dosage, indicating the safety of nanoprobes.

Discussion

In summary, the current study proposed an inflammation nanoprobe-based molecular imaging strategy for depression diagnosis. An MRI nanoprobe was constructed by attaching cLABL peptide onto the surface of biocompatible Fe_3O_4 nanoparticles, which was able to specifically visualize the inflammatory region of the depressed brain in vivo. The effectiveness of the nanoprobe was confirmed through a combination of in vitro and in vivo experiments. The results showed that the nanoprobes can specifically target inflamed vascular endothelial cells by interacting with ICAM-1 receptors and accumulate in the inflamed brain tissue of depressed mice. The reliability of the imaging results was also verified by ex vivo histological analysis. Interestingly, the brain regions highlighted by the nanoprobe on SWI are consistent with the focus regions that are closely associated with the symptoms of depression reported in previous behavioral and statistical studies. Therefore, this nanoprobe-based MRI strategy enables the visualization of the spatial distribution of inflammation in the brains of mice with depression in vivo for the first time.

In our previous work, nanoprobe-based MRI was successfully used to obtain anatomical images of the brain. In particular, angiogenesis, anastomosis, or leakage of the vasculature can be accurately visualized using nanoprobe-enhanced MRI[16]. However, accurately diagnosing depression solely through anatomical structural imaging is challenging because most depressed individuals do not exhibit evident organic brain disorders. To address this issue and enable accurate diagnosis of depression, an inflammation-targeting nanoprobe-based molecular imaging strategy has been proposed in the current work. This strategy shifts the imaging focus from nonspecific anatomical structures to specific pathological molecular sources of the depressed brain. By mapping the spatial distribution of inflammation in the brain, it is possible to detect the focal region associated with depression. This breakthrough not only facilitates insight into the biological mechanism underlying depression but also provides a potential target within the depressed brain for the development of anti-inflammatory therapies.

Materials and methods

Construction of nanoprobes

Typically, 0.7 mg of cLABL cyclic peptide with a sequence of cyclo-(1,12)-PenITDGEATDSGC was dissolved in 0.5 mL of Milli-Q water at room temperature. In addition, 0.2 mg of Traut's reagent (2-iminothiolane hydrochloride) was dissolved in 0.2 mL of Milli-Q water. These two water solutions were mixed under stirring for 2 h. After that, 1.0 mL of aqueous solution containing 4.8 mg of PEGylated Fe_3O_4 NPs was quickly added to the mixture, followed by further stirring for 2 h. The resulting nanoprobes were purified by ultrafiltration with 1× phosphate buffered saline (PBS) using a 30 kDa MWCO centrifugal filter (Millipore YM-30) and stored at 4 °C.

Characterization of nanoprobes

TEM images of the probes and the control particles were acquired using a JEM-2100 transmission electron microscope operating at an acceleration voltage of 200 kV. The particle size was determined by averaging at least 100 nanoparticles per sample. DLS measurements were performed at a temperature of 298 K using a Nano ZS instrument (Malvern) equipped with a solid-state He–Ne laser ($\lambda = 632.8$ nm). The Fe contents of different samples were determined through a spectrophotometric analysis method after eroding the Fe_3O_4 nanoparticles with concentrated hydrochloric acid. The absorption of the aqueous solutions of nanoprobes were measured on a UV−Vis spectrophotometer (Thermo, MULTISKAN GO).

Cell binding affinity evaluation

HUVECs were seeded in a 48-well cell culture plate and then cultured overnight to facilitate firm adherence. Then, half of the cells were cultured with a medium containing LPS (10 μg/mL) for 12 h for activation, while the other cells were cultured with a normal medium. Subsequently, the cells were treated with either nanoprobes or PEGylated Fe_3O_4 nanoparticles (100 μg/mL of Fe) and incubated for 6 h. After co-incubation, the cells were rinsed with PBS buffer to remove the free particles and subjected to Perl's Prussian blue staining. The stained cells were observed using a fluorescence microscope (Leica DMI 3000B).

Cytotoxicity evaluation

The cytotoxicity of the nanoprobes was evaluated using CCK-8 assays. Briefly, HUVECs were seeded into a 96-well cell culture plate at a density of 5000 cells per well and cultured overnight to allow for adhesion. After that, nanoprobes with different Fe concentrations were added to the wells. After coincubation for 24 h, the supernatant of each well was carefully decanted. The new culture media was added and the following incubation lasted for another 24 h. After that, the cells in each well were treated with CCK-8 for 4 h, and the optical density of each well at 450 nm was measured using a microplate reader (Thermo, Varioskan Flash).

Hemolysis rate assessment

Blood samples were collected from BALB/c mice. After that, the red blood cells (RBCs) were collected from a 2 mL blood sample through centrifugation and purified using normal saline (NS). The resulting RBCs were then diluted 1: 4 into NS (negative control), Milli-Q water (positive control), or NS solution containing various concentrations of nanoprobes. These mixtures were kept in the dark for 4 h at 37 °C and then centrifuged at 3000 rpm for 5 min. Subsequently, the absorbance at 541 nm of the supernatant from each sample was measured by a microplate reader (Thermo, Varioskan Flash).

The hemolysis rate was calculated by the following equation:

$$\text{Hemolysis rate} = \frac{D_t - D_b - D_{nc}}{D_{pc} - D_{nc}} \times 100\%$$

where D_t, D_b, D_{nc} and D_{pc} are the absorbance of the supernatant from the tested sample, the corresponding nanoprobe solution background without RBCs, the negative control and the positive control, respectively.

Animal model establishment

Male C57BL/6J mice at the age of 7–8 weeks were purchased from Joinn Laboratories, Inc. (Suzhou, China; license No. SCXK (Su) 2020-0009). The CUMS-induced depression mouse models, together with behavioral tests, including the sucrose preference test (SPT), open field test (OFT), and tail suspension test (TST), were established and conducted according to our previous publication[40]. In brief, C57BL/6J mice were cohoused and received 7 weeks of unpredictable mild stressors, including food deprivation (24 h), forced swimming (10–20 °C, 5 min), water deprivation (24 h), chronic restraint stress (CRS) (6 h), 45° cage tilt (24 h), clipping the tail (1 min), a damp cage (200 mL of water in the sawdust bedding, 7 h), foot shock (1.75 mA, 5 min), and overnight illumination (12 h). The mice in the experimental group ($n = 5$) were randomly exposed to one of the stressors every day, with no repetition of the stressor within a seven-day period. The mice in the control group ($n = 5$) were cohoused and were not subjected to any of the stressors, and were only handled 5 minutes per day. All these mice lived under the same comparable environmental conditions. Following the CUMS procedure, behavioral tests were conducted on each mouse.

In vivo MRI studies

The brain MRI studies were acquired on a 7.0 T animal MRI scanner (Bruker BioSpec70/20 USR) equipped with a mouse head surface coil. During the MRI experiments, the mice were anesthetized with 2% isoflurane in oxygen-mixed air via a facemask. The nanoprobes were intravenously injected into the tail vein at a dose of 10 mg Fe per kg body weight. The MR images were obtained at specific time points as designed.

Detailed parameters of different sequences:

T_1WI: repetition time (TR) = 500 ms, echo time (TE) = 5.58 ms, field of view (FoV) = 23 × 20 mm, matrix (MTX) = 177 × 154, slice thickness = 0.5 mm.

T_2WI: TR = 3000 ms, TE = 40 ms, FoV = 23 × 20 mm, MTX = 177 × 154, slice thickness = 0.5 mm.

T_2*WI: TR = 1393.82 ms, TE = 3.32 ms, FoV = 23 × 20 mm, MTX = 177 × 154, slice thickness = 0.5 mm.

SWI: TR = 480 ms, TE = 7.65 ms, FoV = 23 × 20 mm, MTX = 177 × 154, slice thickness = 0.5 mm.

Histological analysis

After MRI studies, the mice were sacrificed, and their brain tissue was extracted, fixed, and sliced. Then, adjacent slices were selected for H&E, IL-6, TNF-α, eNOS, and VEGF staining.

Additionally, the major organs of the mice, including the heart, liver, spleen, lung, and kidney, were harvested and subjected to H&E staining.

All animal experiments were approved by the *Institutional Animal Care and Use Committee at Shanghai Jiao Tong University (A2021076)* and the *Peking University Institutional Animal Care and Use Committee (LA2019083)*.

Acknowledgements

This work was supported by the NSFC (82102679, 81974357, 22177009), the Postdoctoral Science Foundation of China (2021M700931), the Natural Key Research and Development Program of China (2022YFC2009700), the Guangzhou Municipal Science and Technology Program (202206010197), and the Fundamental Research Funds for the Central Universities of China (buctrc201934). The authors also appreciate the availability of medical image elements from Servier Medical Art (https://smart.servier.com) under the CC BY 3.0 license.

Author details

[1]Department of Rehabilitation Medicine, Guangzhou First People's Hospital, School of Medicine, South China University of Technology, 510180 Guangzhou, Guangdong, China. [2]College of Life Science and Technology, Beijing University of Chemical Technology, 100029 Beijing, China. [3]Shanghai Key Laboratory of Psychotic Disorders, Shanghai Mental Health Center, Shanghai Jiao Tong University School of Medicine, 200030 Shanghai, China. [4]Department of Neurology, West China Hospital, Sichuan University, 610000 Chengdu, Sichuan, China. [5]Department of Psychiatry, and National Chengdu Center for Safety Evaluation of Drugs, West China Hospital, Sichuan University, 610041 Chengdu, Sichuan, China. [6]Key Laboratory for Quality Evaluation of Bulk Herbs of Hunan Province, Hunan University of Chinese Medicine, 410208 Changsha, Hunan, China. [7]Guangzhou Key Laboratory of Aging Frailty and Neurorehabilitation, 510180 Guangzhou, Guangdong, China

Author contributions

P.Z. and J.G. contributed equally to this work. P.Z. designed and conducted most of the experiments under the guidance of Y.L. J.G. established the mouse models of depression. N.Z. and W.L. helped with the MRI experiments. L.Z. and Y.W. assisted with the synthesis of materials. X.L. and X.L. helped establish the animal model. Z.S., M.Q., and Y.H. participated in the discussion regarding the characterization of the materials and the pathological analysis. All authors discussed the results and commented on the manuscript.

Conflict of interest

The authors declare no competing interests.

Publisher's note

Springer Nature remains neutral with regard to jurisdictional claims in published maps and institutional affiliations.

Supplementary information The online version contains supplementary material available at https://doi.org/10.1038/s41427-023-00505-9.

Received: 12 April 2023 Revised: 8 September 2023 Accepted: 13 September 2023.
Published online: 27 October 2023

References

1. Goolsby, M. J. Screening, diagnosis, and clinical care for depression. *J. Am. Acad. Nurse Pract.* **14**, 286–288 (2002).
2. Malhi, G. S. & Mann, J. J. Depression. *Lancet* **392**, 2299–2312 (2018).
3. Rahim, T. & Rashid, R. Comparison of depression symptoms between primary depression and secondary-to-schizophrenia depression. *Int. J. Psychiatry Clin. Pract.* **21**, 314–317 (2017).
4. Iglay, K. et al. Diagnosis and treatment delays among elderly breast cancer patients with pre-existing mental illness. *Breast Cancer Res. Treat.* **166**, 267–275 (2017).
5. Matza, L. S., Rajagopalan, K. S., Thompson, C. L. & de Lissovoy, G. Misdiagnosed Patients With Bipolar Disorder. *J. Clin. Psychiatry* **66**, 1432–1440 (2005).
6. Choe, C. J., Emslie, G. J. & Mayes, T. L. Depression. *Child Adolesc. Psychiatr. Clin. North Am.* **21**, 807–829 (2012).
7. Lowe, B., Unutzer, J., Callahan, C. M., Perkins, A. J. & Kroenke, K. Monitoring depression treatment outcomes with the patient health questionnaire-9. *Med. Care* **42**, 1194–1201 (2004).
8. Williams, J. W. Jr., Stellato, C. P., Cornell, J. & Barrett, J. E. The 13- and 20-item Hopkins Symptom Checklist Depression Scale: psychometric properties in primary care patients with minor depression or dysthymia. *Int. J. Psychiatry Med.* **34**, 37–50 (2004).
9. Zigmond, A. S. & Snaith, R. P. The hospital anxiety and depression scale. *Acta Psychiatr. Scand.* **67**, 361–370 (1983).
10. Mouchabac, S. Severe depression: pharmacological treatments. *L"Encephale* **35**, S319–S324 (2009).
11. Bowden, C. L. A different depression: clinical distinctions between bipolar and unipolar depression. *J. Affect. Disord.* **84**, 117–125 (2005).
12. Zhang, P. et al. Theranostic nanoparticles with disease-specific administration strategies. *Nano Today* **42**, 101335 (2022).
13. Jing, L. & Zhang, P. Nanoprobes for visualization of cancer pathology in vivo. *Acta Chim. Sin.* **80**, 805 (2022).
14. He, F. et al. Red blood cell membrane-coated ultrasmall NaGdF4 nanoprobes for high-resolution 3D magnetic resonance angiography. *ACS Appl. Mater. Interfaces* **14**, 26372–26381 (2022).
15. Qiao, R. et al. Recent advances in molecular imaging of atherosclerotic plaques and thrombosis. *Nanoscale* **12**, 8040–8064 (2020).
16. Zhang, P. et al. Simultaneous identifying the infarct core, collaterals, and penumbra after acute ischemic stroke with a low-immunogenic MRI nanoprobe. *Mater. Des.* **233**, 112211 (2023).
17. Zhang, P. et al. Predicting thrombolytic haemorrhage risk of acute ischemic stroke through angiogenesis/inflammation dual-targeted MR imaging. *Nano Today* **48**, 101707 (2023).

18. Du, Y. et al. Ultrasmall iron-gallic acid coordination polymer nanodots with antioxidative neuroprotection for PET/MR imaging-guided ischemia stroke therapy. *Exploration* **3**, 20220041 (2023).
19. Miller, G. E., Stetler, C. A., Carney, R. M., Freedland, K. E. & Banks, W. A. Clinical depression and inflammatory risk markers for coronary heart disease. *Am. J. Cardiol.* **90**, 1279–1283 (2002).
20. Dantzer, R., O'Connor, J. C., Freund, G. G., Johnson, R. W. & Kelley, K. W. From inflammation to sickness and depression: when the immune system subjugates the brain. *Nat. Rev. Neurosci.* **9**, 46–56 (2008).
21. Thomas, A. J. et al. Elevation in late-life depression of intercellular adhesion molecule-1 expression in the dorsolateral prefrontal cortex. *Am. J. psychiatry* **157**, 1682–1684 (2000).
22. Sakamoto, S. et al. Inflamed brain: targeting immune changes and inflammation for treatment of depression. *Psychiatry Clin. Neurosci.* **75**, 304–311 (2021).
23. Zou, B., Miao, C. & Chen, J. Depression and perceived stress, but not anxiety, are associated with elevated inflammation in an obese adult population. *Risk Manag. Healthc. Policy* **13**, 1489–1497 (2020).
24. Miller, A. H. & Raison, C. L. The role of inflammation in depression: from evolutionary imperative to modern treatment target. *Nat. Rev. Immunol.* **16**, 22–34 (2016).
25. Goldsmith, D. R., Bekhbat, M., Mehta, N. D. & Felger, J. C. Inflammation-related functional and structural dysconnectivity as a pathway to psychopathology. *Biol. Psychiatry* **93**, 405–418 (2023).
26. Yusuf-Makagiansar, H. et al. Sequence recognition of alpha-LFA-1-derived peptides by ICAM-1 cell receptors: inhibitors of T-cell adhesion. *Chem. Biol. Drug Des.* **70**, 237–246 (2007).
27. Xu, C. R., Yusuf-Makagiansar, H., Hu, Y., Jois, S. D. S. & Siahaan, T. J. Structural and ICAM-1-docking properties of a cyclic peptide from the I-domain of LFA-1: an inhibitor of ICAM-1/LFA-1-mediated T-cell adhesion. *J. Biomol. Struct. Dyn.* **19**, 789–799 (2002).
28. Zhang, P. et al. Nanoprobe based on biominerals in protein corona for dual-modality MR imaging and therapy of tumors. *ACS Nano* **17**, 184–196 (2023).
29. Zhang, P. et al. Quantitative mapping of glutathione within intracranial tumors through interlocked MRI signals of a responsive nanoprobe. *Angew. Chem. Int. Ed.* **60**, 8130–8138 (2021).
30. Fulcher, N., Tran, S., Shams, S., Chatterjee, D. & Gerlai, R. Neurochemical and behavioral responses to unpredictable chronic mild stress following developmental isolation: the zebrafish as a model for major depression. *Zebrafish* **14**, 23–34 (2017).
31. Caligiuri, M. P. et al. Striatopallidal regulation of affect in bipolar disorder. *J. Affect. Disord.* **91**, 235–242 (2006).
32. Coccurello, R. Anhedonia in depression symptomatology: appetite dysregulation and defective brain reward processing. *Behav. Brain Res.* **372**, 112041 (2019).
33. Chung, S. et al. Electroconvulsive shock increases SIRT1 immunoreactivity in the mouse hippocampus and hypothalamus. *J. ECT* **29**, 93–100 (2013).
34. Magdaleno-Madrigal, V. M. et al. Acute deep brain stimulation in the thalamic reticular nucleus protects against acute stress and modulates initial events of adult hippocampal neurogenesis. *Behav. Brain Res.* **314**, 65–76 (2016).
35. Chrapko, W. E. et al. Decreased platelet nitric oxide synthase activity and plasma nitric oxide metabolites in major depressive disorder. *Biol. Psychiatry* **56**, 129–134 (2004).
36. Warner-Schmidt, J. L. & Duman, R. S. VEGF is an essential mediator of the neurogenic and behavioral actions of antidepressants. *Proc. Natl Acad. Sci. USA* **104**, 4647–4652 (2007).
37. Lippi, G., Montagnana, M., Favaloro, E. J. & Franchini, M. Mental depression and cardiovascular disease: a multifaceted, bidirectional association. *Semin. Thromb. Hemost.* **35**, 325–336 (2009).
38. Abbaspour, N., Hurrell, R. & Kelishadi, R. Review on iron and its importance for human health. *J. Res. Med. Sci.* **19**, 164–174 (2014).
39. Meng, F. et al. Lysosomal iron recycling in mouse macrophages is dependent upon both LcytB and Steap3 reductases. *Blood Adv.* **6**, 1692–1707 (2022).
40. Guan, J. et al. Splenectomy does not affect mouse behaviors. *Neural Regen. Res.* **18**, 1789–1794 (2023).